3D-Printed Self-Folding Electronics

Subramanian Sundaram,[*,†,‡] David S. Kim,[†] Marc A. Baldo,[‡] Ryan C. Hayward,[§] and Wojciech Matusik[†,‡]

[†]Computer Science and Artificial Intelligence Laboratory and [‡]Electrical Engineering and Computer Science Department, Massachusetts Institute of Technology, Cambridge, Massachusetts 02139, United States

[§]Polymer Science and Engineering Department, University of Massachusetts, Amherst, Massachusetts 01003, United States

S Supporting Information

ABSTRACT: Self-transforming structures are gaining prominence due to their general ability to adopt programmed shapes each tailored for specific functions. Composites that self-fold have so far relied on using the stimuli−responsive mechanisms focusing on reversible shape change. Integrating additional functions within these composites can rapidly enhance their practical applicability; however, this remains a challenging problem. Here, we demonstrate a method for spontaneous folding of three-dimensional (3D)-printed composites with embedded electronics at room temperature. The composite is printed using a multimaterial 3D-printing process with no external processing steps. Upon peeling from the print platform, the composite self-shapes itself using the residual forces resulting from polymer swelling during the layer-by-layer fabrication process. As a specific example, electrochromic elements are printed within the composite and can be electrically controlled through its folded legs. Our shape-transformation scheme provides a route to transform planar electronics into nonplanar geometries containing the overhangs. Integrating electronics within complex 3D shapes can enable new applications in sensing and robotics.

KEYWORDS: self-folding, multimaterial 3D-printing, flexible electronics, electrochromic pixels, robotics

INTRODUCTION

Programmable matter and self-assembled structures have highlighted a range of applications that unify physical shape and overall function.[1,2] Emerging advances in robotics,[3] photovoltaics,[4] antennas,[5] biomimetic imagers,[6] and inertial measurement units[7] present a compelling class of devices where electronics have evolved to nontraditional complex architectures. Adapting contemporary planar electronics that have high performance to three-dimensional (3D) geometries has proved to be a challenging problem. This is currently being tackled using a variety of techniques, such as using droplet wetting to induce self-folding,[4] manual folding of silicon pieces with interlocks,[7] and compressive buckling of thin silicon membranes bonded on prestretched materials.[8] The general approach thus far is to create the electrical device on a planar silicon wafer using microfabrication techniques and subsequently shape it using different methods. These shaping techniques have the advantage of being directly applicable to planar-fabricated silicon-based electronics. However, they tend to be device specific, constrained in possible geometries, or not easily scalable. A process that creates an electrical function within a complex 3D structure seamlessly is of significant practical importance, and is therefore an active area of research.

Outside the confines of traditional electronic device fabrication, a broad set of origami- and kirigami-inspired techniques have been extensively explored as the potential routes to fabricate complex 3D structures thus far.[2,3,9−15] Demonstrations of material folding have spanned several orders of magnitude in length scales, utilizing a disparate set of mechanisms including[9] controlled buckling,[8] shape-memory effect in composites,[10,11] pneumatically driven transformations,[12] thermally controlled swelling in hydrogels,[13] photo-induced folding and manipulation,[14−18] residual stress-induced curling,[19] and controlled formation of creases.[20] Recently, additive manufacturing has also been used to create 3D structures using shape transformation (four-dimensional (4D)-printing).[21−23] This is in part driven by the high-speed capabilities of 3D-printing[24] and the ability to assemble a set of diverse materials simultaneously.[25−28] Folding flat, printed designs into complex structures has additional benefits over directly printing the final 3D structure, typically in the overall fabrication speed, cost, and ease of scaling. Furthermore, when solvent-based inks are used (as is typical for a majority of electrically important materials), folded geometries may not be directly 3D-printed due to challenges from droplet spreading and nonuniform film thicknesses. This has generated considerable recent interest in 4D-printing; structures that change dynamically allows the shape to be controlled over

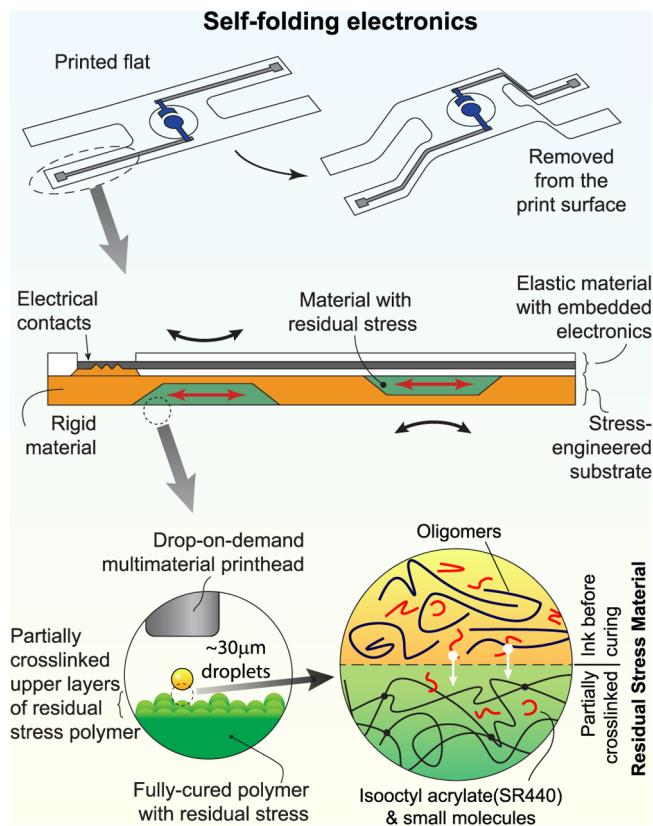time.[29−34] Although there have been attempts to embed packaged electronics inside 3D-printed structures[35,36] to improve their overall functionality,[37] achieving fully 3D-printed electronics that self-fold is a current challenge. As a first step in this direction, Zarek et al. have recently inkjet-printed conductors on top of flattened 3D-printed shapes that can then be restored to their original shapes using the shape-memory effect.[38] Similarly, electrically conductive shape-memory materials have also been 3D-printed via direct ink writing.[39] Despite the tremendous interest in shape transformation in 3D-printed structures, there are several practical challenges that exist in expanding these structures to include printed electronic devices. The two common classes of mechanisms used for self-folding in 3D-printed structures are based on the temperature-controlled shape-memory effect in polymers and the controllable swelling of hydrogels in water and other liquids.[40] The main focus of these approaches is the ability to achieve reversible self-folding, which is a significant advantage. The required stimuli, that is, temperature cycling and immersion in liquids, however, may not desirable for use with electronic devices. This is particularly relevant if the electrically active materials of the self-shaping composite may degrade with temperature cycling or exposure to humidity. Controllable folding with the ability to engineer stress at multiple positions is more favorable for electronics applications that do not require reversible shape change. Recently, Ding et al. reported a folding method using a temperature input in a system of polymers with different coefficients of thermal expansion to accelerate folding based on an inbuilt strain.[41] This is an elegant method that can create rapid folds. However, the use of a commercial printer with proprietary inks (that by default uses a flattening roller) makes it challenging to identify the stress creation mechanism. Furthermore, electrically relevant materials cannot be printed with this system, which is the main goal of our work.
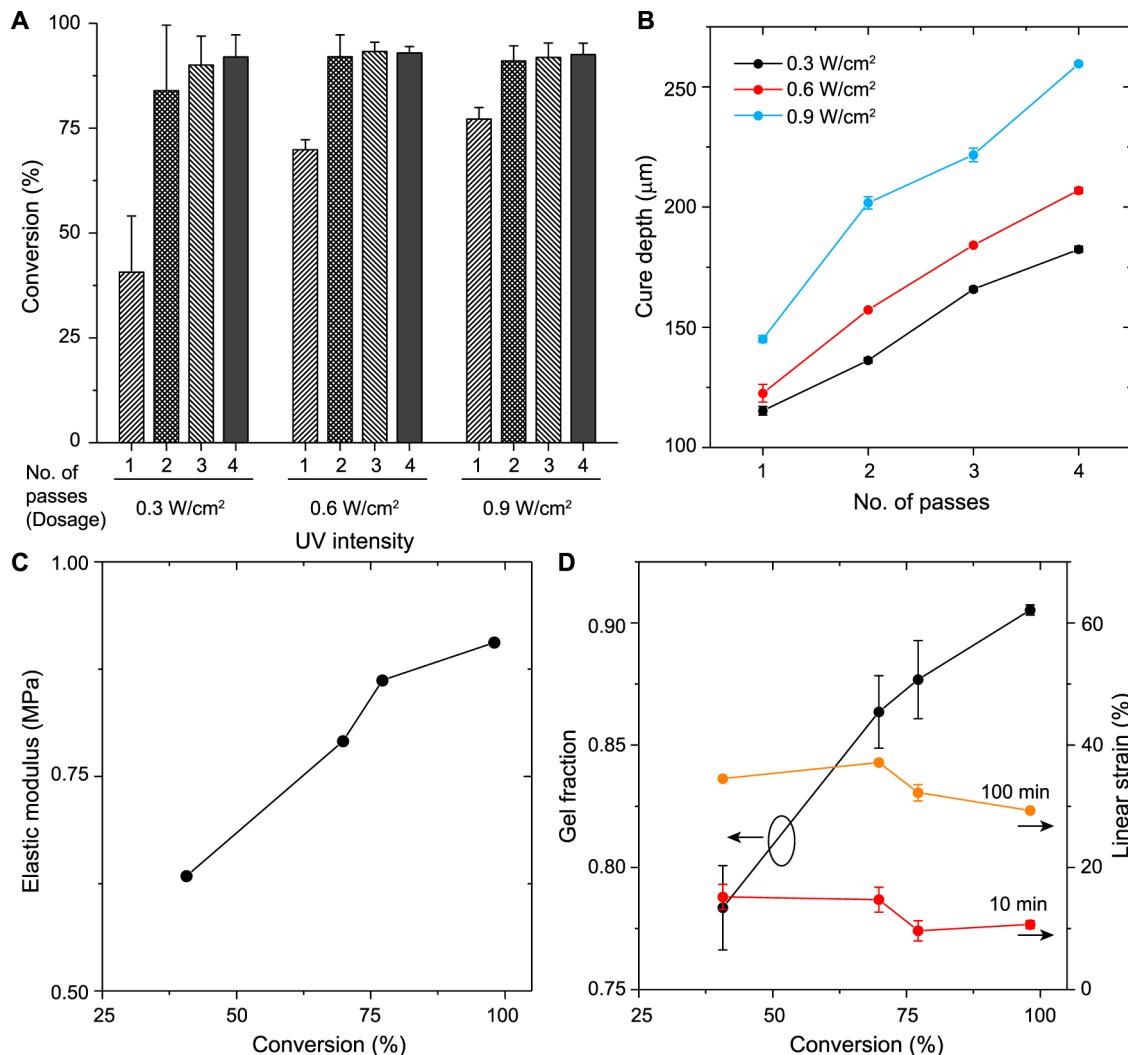
■ RESULTS AND DISCUSSION

Here, we present a new approach of fabricating electronic composites that can self-fold at room temperature. We achieve this by fully 3D-printing the electronic device and the surrounding polymer matrix with locally engineered stress in a single system with no external intervention. A drop-on-demand multimaterial 3D-printing process with a voxel-level control is used to fabricate the structures in this work.[42,43] Upon removing the printed parts from the platform, they self-fold into the preprogrammed 3D structure requiring no other controlled stimulus. Both convex and concave folds are achieved by directly writing the residual stress in select regions of the printed object, as shown in the scheme in Figure 1. To create the residual expanding tendency, we formulate an ink containing acrylate monomers and oligomers that can be cross-linked by UV light (detailed formulation is in Experimental Section). The UV-cured (cross-linked) polymer swells significantly in the starting ink containing small molecules (with pronounced swelling in isooctyl acrylate). Immersion in a monomer solution has been recently used as an external stimulus to expand a low cross-link density polymer.[44] During the layer-by-layer printing process here, each underlying cured layer (∼17 μm in thickness), is automatically exposed to new ink, which diffuses into the partly cross-linked layer below before the UV light passes over it. This causes the material to have an inherent residual stress that forces it to expand when unconstrained (removed from the print platform). This is

Figure 1. Schematic representation of spontaneously folding electronics achieved by multimaterial 3D-printing. The composites containing active electronics, metallic traces, and the substrate are fully 3D-printed. On removing the 3D-printed structure from the print platform, the composite spontaneously folds in a shape based on the locally engineered residual stress, requiring no stimulus at room temperature. At the heart of this scheme is a UV-curable ink containing high-elongation acrylate oligomers and short-chain monomers (such as isooctyl acrylate). As a part of the layer-by-layer inkjet-based 3D-printing process, each previously cured (lightly cross-linked) layer, ∼17 μm thick, is exposed to uncured ink from the subsequent layers. The small molecules from the ink swell the underlying cured layers and create a local residual stress. Both the circular close-ups shown in the bottom only show the residual stress material before and after curing; the rigid material is not linked to the stress-generation mechanism. The role of each ink component is shown in Figure S1. This material, which is used to directly write residual stress in a volume, is combined with rigid UV-curable acrylates to create both concave and convex folds of the desired angles by controlling the material placement and geometry in the design. The active electronics are linked by a stretchable conductor all printed within the same system.

illustrated in the bottom right of the scheme in Figure 1, where the ink before curing is shown in yellow and the lightly cross-linked upper layers are shown in green (the colors correspond to the same residual stress material before and after curing).

At the heart of this self-folding scheme is the swelling of the cross-linked polymer in its starting ink components, and the ability to deposit multiple materials. To verify that the layer-by-layer process that facilitates swelling is indeed responsible for the introduction of the residual stress, the ink is poured in a mold and cured in a single step using a high-intensity (14 W cm^{-2} at 365 nm, UV fusion) broadband UV source. Upon release from the mold, the cured piece does not expand but instead shrinks slightly as a result of the formation of cross-
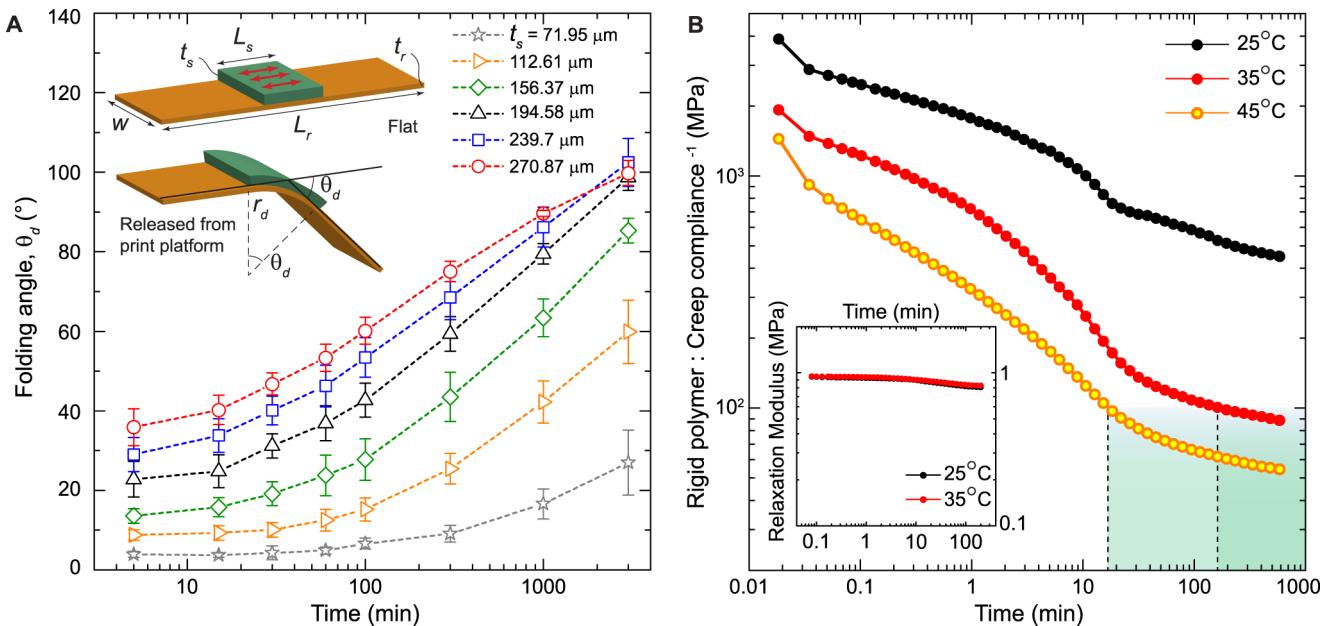
Figure 2. Residual stress polymer and process characterization. (A) The double-bond conversion percentage is calculated as a function of the UV light intensity and the number of curing passes from the Fourier transform infrared (FTIR) attenuated total reflection (ATR) measurements on the surface of the samples (three samples for each data point). The absorbance values corresponding to the reactive double bond "$-CH=CH_2$" group are normalized with respect to the "$-COO-$" group to obtain the reaction conversion (40). The sample FTIR spectra are shown in Figure S2. (B) Plot of the cure depth measured as a function UV light intensity and the number of passes. (C) Elastic modulus values are measured for the samples after one UV curing pass at various light intensities (0.3, 0.6, and 0.9 W cm^{-2} using the printer and ~14 W cm^{-2} using a high-intensity broadband source, UV fusion). (D) Measured linear expansion in one dimension as a function of double-bond conversion for different swelling times (samples are ~125 μm thick). The samples are prepared using single curing passes with varying UV light-emitting diode (LED) intensities. As printed, the samples shrink by <1% typically. These samples with one-shot curing are expected to show isotropic swelling. The plot also shows the measured gel fraction of these samples.

links. To quantify the swelling tendency of the cross-linked polymer in the ink components, the samples (cured in a single step) are allowed to swell by immersion in each of the individual ink components. The swelling results (Figure S1) show that SR440 (isooctyl acrylate) plays a dominant role (causing ~10% expansion in each dimension of a 1 mm thick slab, after 1 h), whereas all of the other individual components lead to negligible swelling over the same time. This is in part due to the nature of the side chains of the acrylate components. SR440, SR504, and SR313B include an isooctyl group (C_8H_{17} chain), ethoxylated nonyl-phenol group ($C_{23}H_{39}O_4$ group, which includes a phenol group), and a dodecyl group ($C_{12}H_{25}$ chain; methacrylate), respectively. It is expected that SR440 diffuses the most due to its low molecular weight and shortest side chain, although multiple other factors may be relevant. The expected diffusion times are explained further in Figure S1. It is

important to note that during the actual printing process, the uppermost printed layers are exposed to one pass of the 0.9 W cm^{-2} UV source before exposure to the fresh ink. Therefore, the diffusion is expected to be further enhanced in the printing process compared with the single-step fully cross-linked samples. After small molecules diffuse into the underlying layers, they are cross-linked into the existing network with the subsequent UV-curing passes.

To gain further insights into the state of the residual stress polymer, we measured the Fourier transform infrared (FTIR) attenuated total reflection (ATR) spectra for the samples cured with various UV intensities and number of curing passes in the printer. The reactive double conversion is measured by normalizing the absorption peak of the "$-CH=CH_2$" group with respect to the "$-COO-$" group[40] (the sample FTIR spectra are shown in Figure S2 and described in Experimental
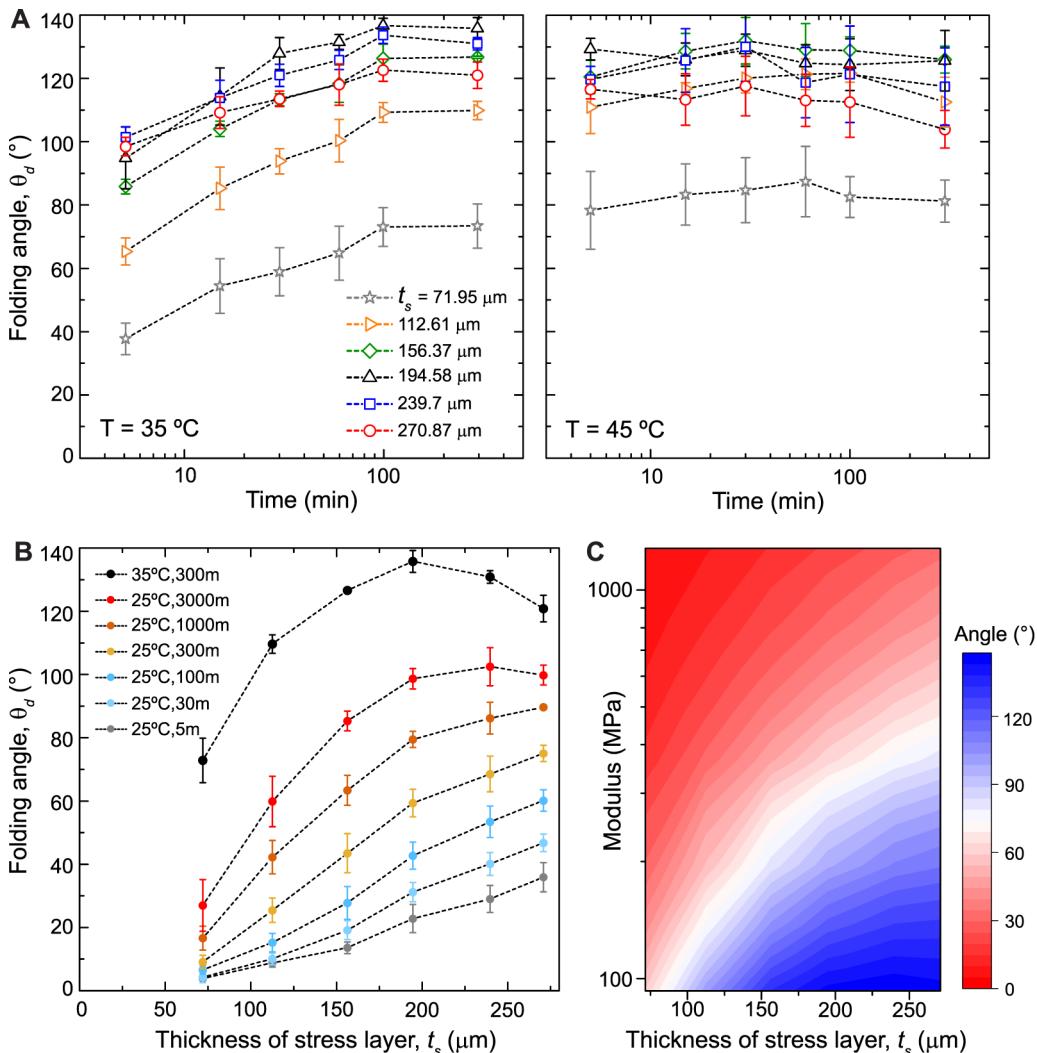
Figure 3. Temporal characteristics of the bilayer system used for creating folds. (A) Inset shows a bilayer stack where the material with the residual stress (green, called residual stress material in text) causes the underlying substrate made of the rigid material to bend. The plot shows the time evolution of θ_d, the bending angle at standard room temperature (25 °C) once the sample is removed from the print platform. The different curves show the bending angle as a function of time for varying thickness of the material with residual stress, t_s. For these tests, the thickness of the rigid polymer is $t_r = 99.9 \pm 4.3$ μm, width $W = 3.25$ mm, and length $L_r = 15$ mm and $L_s = 4$ mm. The folding angle does not settle even after 3000 min. (B) The plot shows the inverse of the creep compliance of the rigid material at 25, 35, and 45 °C. The material shows a rapid increase in the compliance until ~30 min, after which the increase in creep compliance settles to a slower rate. The modulus drops by more than 1 order of magnitude between the start and 10 h into the creep test. With the rigid material having a glass transition temperature (T_g) close to the room temperature, the inherent stiffness of the material drops drastically as the temperature increases above 25 °C. The shaded region shows the time it takes for the inverse creep compliance to drop below 100 MPa. The inset shows the relaxation modulus of the stress layer material. The relaxation modulus shows a negligible drop after 200 min (of the stress-relaxation experiment). Further, there is no significant change in the base stiffness of the material as the temperature is increased to 35 °C because the material is well into the rubbery regime. The glass transition measurements for the two materials are included in Figure S3.

Section). From Figure 2A, it is observed that the double-bond conversion of the lightly cross-linked layer (one pass with the default 0.9 W cm^{-2} intensity source) is ~77%; the samples reach near full double-bond conversion after three passes (from the three samples for each data point). For the measurements in Figure 2A, the light intensity was varied below the default intensity to understand the effect of reduced UV-curing intensity. Here, new material was not added in between the curing passes purely to understand the effect of multiple curing passes. During the printing process, there is a gradient in the received UV dosage going from the uppermost printed surface (latest) to the first printed layers. To perform a controlled study of the equivalent initial strain in the samples without the dosage gradients along the thickness, we performed subsequent measurements of gel fraction and linear strain using single-step cured samples of a controlled thickness. For the thickness of layers to be meaningful, that is, without significant gradients in the cross-link density along the depth, we try to constrain this value below the cure depth at each UV intensity, as shown in Figure 2B. A typical cure depth after one pass of the UV light at 0.9 W cm^{-2} intensity is ~150 μm. Figure 2C shows the measured elastic modulus of the samples after one curing pass. It can be observed that the modulus increases with the cross-link density. To understand the strain in the printed layers, we UV cured multiple samples with one pass of the UV light with different intensities (controlling the double-bond conversion). The measured increase in one dimension (averaged from four individual samples) is plotted as a function of the double-bond

conversion as shown in Figure 2D. In these experiments, the cured samples were soaked in the starting ink of the residual stress material for different amounts of time to control the swelling. It is observed that the resulting strain increases with the swelling time. It is to be noted that these experiments were performed with a spacer of thickness ~125 μm for handling despite this being close to the cure depth at lower UV intensities; the samples with 0.3 W cm^{-2} curing were very fragile and easy to tear. It is worth noting that the diffusion time is proportional to the square of the thickness; a 10 min swelling experiment conducted on a 125 μm sample corresponds to ~10 s of swelling a 17 μm layer. Additionally, the experiments are conducted at room temperature; however, in the actual printing process, the droplets leaving the printhead leave at an elevated temperature and would experience an increase in diffusion. The measured increase in the length can be translated to the isotropic increases in all of the three dimensions for single-pass cured samples swelling in the starting ink. During the printing process, the scenario is different with isotropic stresses only in the in-plane directions but not in the out-of-plane directions.
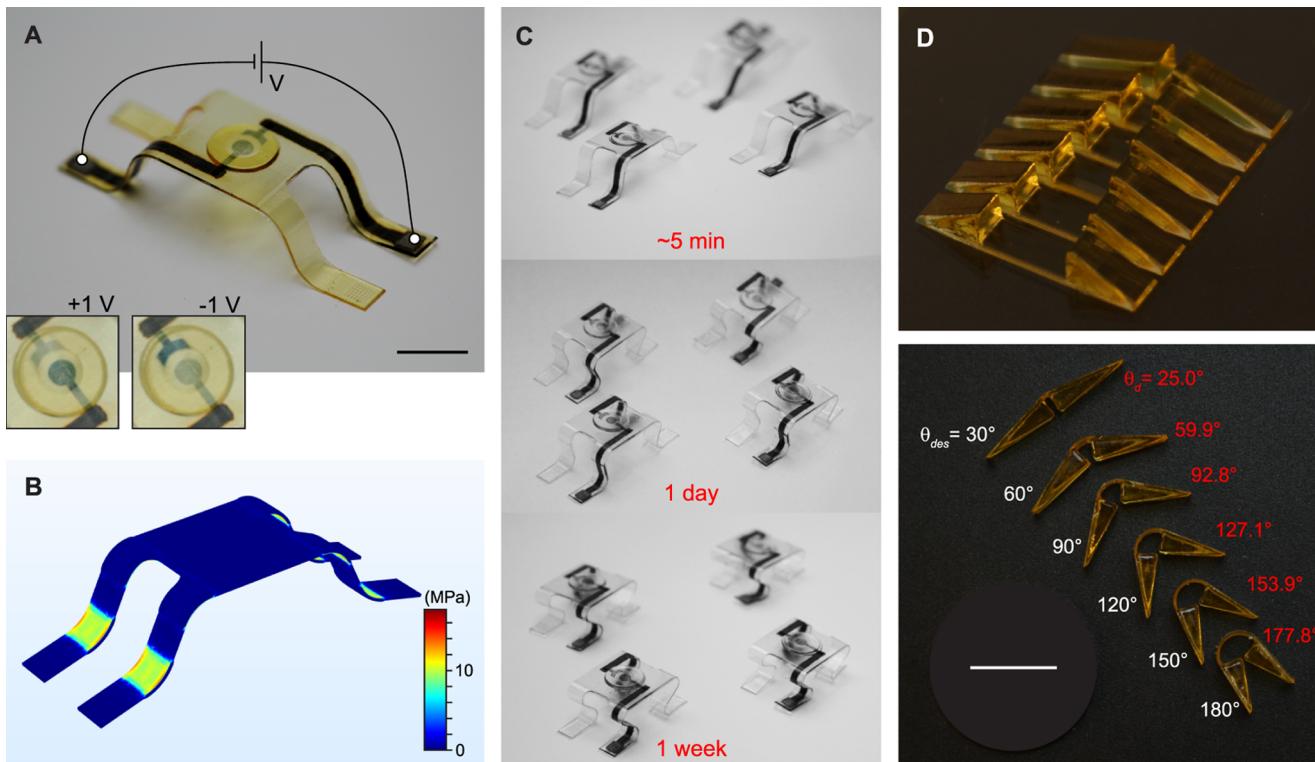
The residual stress material is printed along with a thin, rigid acrylate polymer material (thermoset) in a bilayer configuration to generate folds, as shown in the inset of Figure 3A. The expansion in the stress layer exerts a surface load on the rigid polymer, causing the structure to bend, with a uniform radius of curvature, r_d. To characterize the folding, multiple bilayer structures are 3D-printed and the folding angle is measured as a function of the thickness of the stress layer over time. The

Figure 4. Bilayer characteristics at elevated temperatures and design guidelines. (A) Plots show the time dependence of the folding angle of the bilayer system used for creating folds at 35 and 45 °C. The folding angle shows little variation past 100 min at 35 °C. Samples approach a steady-state folding angle after ∼5 min at 45 °C. (B) The folding angle is shown as a function of the stress layer thickness at various time instants at 25 °C. The black curve shows the saturated folding angle at 35 °C (after 300 min). Note that the optimum thickness of the stress layer for creating larger folds changes with time (due to a larger creep compliance). (C) Finite-element analysis (FEA) predictions of the folding angle based on the geometry and time (or equivalently elastic modulus, from Figure 3B). Comparison with the experimental values and Timoshenko's bilayer model is explained in the Supporting Information and in Figure S5.

thickness of the rigid layer, t_r, is 99.9 ± 4.3 μm, the width, W, is 4 mm, and the stress layer thickness varies from 71.95 to 270.9 μm. The printed samples are peeled from their flat state and kept at a controlled temperature (25 °C). The folding angle, θ_d, is measured as a function of time for multiple designs and shown in Figure 3A, with each point showing measurements from three samples. It is observed that the folding angle increases with the stress layer thickness (in this range) until 1000 min, and the angle continues to increase over time, showing no saturation up to 3000 min. When no stress layer is added (as negative control samples), the rigid layers themselves do not show any noticeable folding over time. To design new structures, understanding this temporal behavior in the folding angle and its relationship with geometry is essential. As a first step to understanding the material behavior at room temperature (25 °C) and establishing its relationship with the glass transition temperature, differential scanning calorimetry (DSC) and dynamic mechanical analysis (DMA) are performed. The glass transition temperatures (T_g) of the rigid material and the

stress layer are identified to be around 50 and −10 °C, respectively, with the rigid material exhibiting a broader glass transition (measurements are in Figure S3). To understand the relaxation time scales in the expanding residual stress polymer, the stress-relaxation measurements are performed using DMA and shown in the inset of Figure 3B. It is observed that the relaxation modulus is ∼0.9 MPa and shows little change with time and temperature, confirming that the material with the residual stress is in a completely rubbery state. The time evolution of the angle is thus more likely attributed to the rigid polymer with its broad glass transition regime and the proximity of T_g to room temperature. To understand the time scale of polymer chain relaxation in the rigid material, creep compliance measurements are performed using DMA, and the results are shown in Figure 3B for 25, 35, and 45 °C. The inverse creep compliance drops by approximately an order of magnitude by 600 min, and the rate of decrease rises as the temperature is brought closer to 50 °C. It is also observed that the drop in the inverse creep compliance slows down beyond

E

Figure 5. Self-folding composites. (A) Image shows an electrochromic element integrated in a spontaneously folding fully printed composite. The composite consists of six materials that are printed simultaneously using no external processing (see Figure S7). The transmission through the electrochromic ink (PEDOT:PSS) can be modulated by applying a voltage as shown in the bottom. Video S1 shows the electrochromic pixel. The stretchable printed conductor provides electrical contacts through the folded legs. Scale bar is 10 mm. (B) Finite-element simulations using the equivalent input strain (0.22) obtained earlier shows a close match to the deformed structure ~5 min after the removal from the print substrate, as shown in (A). The von Mises stress in the structure is seen to be concentrated in the bilayer regions of the legs. (C) Series of photographs shows the change in the folding angles over the course of a week. (D) Printed bilayer structures with folding stops, before removal from the platform (top), and a set of structures after reaching steady-state folding angles. Scale bar is 10 mm. The measured angles are plotted as a function of designed angles in Figure S8.

~20−30 min after the application of the load. To confirm that the change in the folding angle with time is a result of the increasing rigid material (substrate) compliance, we repeat the measurements of the folding angle for multiple designs at elevated temperatures (35 and 45 °C). At these slightly elevated temperatures, the sharper drop in the inverse creep compliance results in larger folds and saturation of the folding angle after 100 and ~10 min at 35 and 45 °C, respectively, for the same set of designs (shown in Figure 4A). It can be seen that the effective modulus of the rigid material falls below ~100 MPa at these time intervals from Figure 3B; a first-order explanation for this threshold is included in the Supporting Information using energy methods. Effectively, as the equivalent elastic modulus of the rigid material (substrate) starts to drop over time, an increasing portion of the residual energy stored in the stress layer (expanding material) is used in deforming (bending) itself. Beyond this threshold modulus of the rigid material, the energy spent in bending the rigid substrate is negligible, and further reduction in its elastic modulus does not result in an increase in the folding angle. It is also evident that at elevated temperatures, increasing the thickness of the stress layer does not necessarily lead to an increase in the folding angles (experimental results in Figure 4A,B; simulation results in Figure S5B and explained in the Supporting Information).

The effective residual energy stored in the stress layer can be obtained from the folding angle measurements. Moreover, the time evolution of the folding angle can be accounted for, purely based on the change in the effective elastic modulus of the rigid material (shown in Figure 3B). Therefore, the folding angle can be mapped as a function of thickness of the stress layer as shown in Figure 4B, where each time instant is mapped to a particular value of the elastic modulus of the rigid material. Given the device geometry and the material properties, the bending angle can be obtained using Timoshenko's model of a bilayer with two linear elastic materials[45,13] as a function of an equivalent initial strain in the expanding material (see the Supporting Information). Here, using finite-element analysis (FEA) on the measured geometry of the printed bilayer devices, we estimated the equivalent isotropic initial strain in the material to be ~0.22; the simulation procedure is elaborated and the results are compared with the experimentally measured values and Timoshenko's equation in Figure S5. FEA is used to obtain predictions of the folding angle based on the geometry and time as shown in Figure 4C; the correlation between the effective elastic modulus of the rigid material and time is obtained from Figure 3B. It is expected that the folding behavior is also sensitive to the amount of cross-linking (based on UV curing). The UV intensity of the LED array in the printer at the printing height is 0.9 W cm^{-2}; the effects of excessive UV dosage and high-temperature exposure are discussed in the Supporting Information and shown in Figure S6.

Entire composites are fabricated with a multimaterial printer (six materials in total) to demonstrate the potential for using this material system in self-folding electronic composites. Although active electronics have been printed previously,[42] it is important to recognize that when solvent-based inks are printed, the underlying substrate has to be locally flat to restrict movement of the ink during the printing process. It is therefore challenging to directly print fully folded composites with embedded electronics containing curved structures with overhangs. The stress layer and the rigid material are used as the overall mechanical structure and act as a substrate for the other materials: an elastic layer to control the surface energy, reactive silver ink[46] to make the contacts, poly(3,4-ethylenedioxythiophene):poly(styrene sulfonate) (PE-DOT:PSS), and an electrolyte. The stress layer, the rigid material, and the elastic material are UV cured. The convective heater is used with the reactive silver ink to initiate precipitation of the silver nanoparticles and to evaporate the solvent in the PEDOT:PSS layers. In the final device, the applied voltage controls the movement of metal ions from the electrolyte into the PEDOT:PSS channel. This de-dopes the PEDOT:PSS, leading to a change in the optical contrast and electrical conductivity.[47] The design of the composite and the cross-sectional schematic are described in the Supporting Information and Figure S7. Figure 5A shows a printed self-folding structure with an embedded electrochromic pixel using the aforementioned inks, 5 min after removal from the print platform; Figure S7B shows a printed device before and a week after being removed from the platform. The finite-element simulation of the folded structure (without any fitting parameters) shows a good match, with most of the stress concentrated in the rigid material at the bilayer regions. The elastic modulus of the rigid material 5 min after the application of the load (~1279 MPa, from Figure 3B) and ε = 0.22 are used for the results shown in Figure 5B. The electrochromic structure utilizes the optical contrast between the oxidized and reduced states of the PEDOT:PSS film that can be electrically controlled. The stretchable conductor is subjected to compressive and tensile strains in the adjacent folds in two legs that provide electrical contacts. The precipitated silver nanoparticle layers that make up the stretchable conductor remain conductive until the mechanical breakage of the underlying polymer (up to ~40% strain).[42] When the polarity of the control voltage (1 V) is switched, the transmission through the pixel changes, as shown in the inset at the bottom in Figure 5A; a video recorded a day after the device was removed from the substrate is shown in Video S1.

The shape of the composite changes over time, and Figure 5C shows the shape change in an array of prints over the course of 1 week. Although the shape change over time may be desirable in certain applications, it is equally desirable to achieve fixed folds at controllable angles irrespective of the external temperature fluctuations. Mechanical stops can be designed on either side of the bilayer stack for this purpose, as shown in Figure 5D (top). On removing the structures from the substrate, and even when exposed to a hot air gun set to 100 °C for 1 min, the folds stop at predesigned angles, as shown in the bottom. The desired stop angles can be designed and controlled accurately based on the geometry (Figure S8). At first, it appears that only small folding angles are achievable at room temperature (25 °C), and that the folding angle continues to change for at least over 2 days (Figure 3A). It is important to note that only r_d, the radius of curvature, is

constrained, that is, larger folding angles can be obtained by scaling L_s. Mechanical stops can be designed to limit folding at the desired radius of curvature (time). If the materials in the composite do not degrade with a small temperature increase, a small radius of curvature or accelerated folding can be achieved (at 35 °C). While generating folds from the planar composites, it is expected that the achievable geometries are analogous to the shapes from origami. The geometric limitations here come from the achievable radius of curvature and the temporal characteristics elaborated earlier. Flattening a fold typically takes about ~0.1 N of force for the structures in our work; Figure S9 includes the experiments on unfolding forces and Video S2 shows the related videos. It is worth noting that all of the samples in this work rely on the residual stress created in the in-plane printing directions for folding. During the printing process, the uppermost printed layers are unconstrained on the upper side and free to swell in the z direction. To control the magnitude of the equivalent inbuilt strain, several approaches exist. The amount of swelling can be increased by increasing the layer printing time, leading to a larger residual stress. Additionally, a multimaterial process like ours allows the use of multiple inks with widely different swelling ratios, allowing excellent spatial resolution in prescribing residual stress.

■ SUMMARY

In summary, the residual stress-based folding method described here provides a new route to design 3D shapes folded from planar polymer composites at room temperature. Furthermore, the ability to control the degree of folding based on the design geometry enables designs that are tolerant to small temperature changes. The formulated inks and the corresponding material characterization results here presents a complete toolkit required to design, simulate, and fabricate new geometries. The demonstrated self-folding electronic composite, fabricated without using any external processing, is expected to inspire electronics in new form factors. The addition of actuation mechanisms can further improve the utility of these composites in applications in robotics and human−machine interfaces.

■ EXPERIMENTAL SECTION

Three-dimensional-Printing Process. The custom built drop-on-demand multimaterial 3D printer and its typical use are as described in a paper;[42] details of the system architecture are in a report.[43] The specific details relevant in this work are summarized here. The inkjet printheads are mounted on a carriage with the material feeding system, UV-curing LEDs (wavelength = 365 nm, intensity ~ 0.9 W cm^{-2}), and forced convection heater (ceramic heating element is maintained at 325−350 °C). The feeding system heats the UV-curable inks to reduce the viscosity to the printable range and connects them to a heated printhead (70 °C). The solvent-based inks are not heated and are directly connected to the printhead at room temperature. The model to be printed is designed as an STereoLithography file (STL) and a custom voxelizer is used to breakdown the geometry to a 3D arrangement of voxels. Each layer of the print file is completed in several inkjet printing passes (each pass takes 1−5 s). After each printing pass, the newly printed droplets are automatically UV cured in the case of UV-curable polymer inks, or subjected to heating passes in the case of solvent inks. The typical in-plane resolution of the printing system is 35 μm; the dimensional properties and the resolution are described in detail elsewhere.[42] Multiple materials can be printed simultaneously in each pass of the printer. All of the printing parameters, such as the pressure in the feeding system and the number of heating/UV-curing passes, are controlled from a printer configuration file and the printer user interface.

Ink Preparation. All of the inks used in this work are prepared by mixing commercially available components. The material with the residual stress is prepared by mixing 53.1 wt % CN3105 (low-viscosity acrylic oligomer; Sartomer), 18.8 wt % SR440 (isooctyl acrylate; Sartomer), 17.7 wt % SR504 (ethoxylated nonyl-phenol acrylate; Sartomer), 8.85 wt % genomer 4215 (aliphatic urethane acrylate; Rahn USA Corp.), 1 wt % Irgacure 819 (bis(2,4,6-trimethylbenzoyl)-phenylphosphineoxide; BASF, Germany), 0.5 wt % 2-isopropylthioxanthone (ITX; Rahn USA Corp.), and 0.05 wt % methoxyphenol (MEHQ; Sigma-Aldrich). The different components are homogenized and left to mix overnight using a magnetic stirrer. Finally, the ink is filtered using a 1 μm filter and degassed using a vacuum pump to remove small bubbles. A rigid material ink is obtained by mixing the following components in a similar fashion: 57.8 wt % genomer 1117 (cyclic trimethylolpropane formal acrylate; Rahn USA Corp.), 31.3 wt % genomer 2252/GP25 (bisphenol A epoxy diacrylate in 25% propoxylated glycerol triacrylate; Rahn USA Corp.), 8.8 wt % Miramer M300 (acrylic acid ester; Rahn USA Corp.), 1 wt % Irgacure 819, 1 wt % ITX, and 0.1 wt % MEHQ. The other inks used in the electronic composite—elastic material used to engineer the surface energy, reactive silver ink,[46] PEDOT:PSS ink, and electrolyte ink—are prepared using the previously reported procedure.[42] Typically, all of the inks are optimized for suitable rheological properties (viscosity < 15 mPa s) and used in a drop-in-flight analysis system (jetXpert; ImageXpert Inc., Nashua, NH) to further optimize the waveform for a satellite-free droplet generation.

Material Characterization and Folding Measurements. Mechanical stress–strain tests for the material with residual stress (Figure S4) and controlled deformation in the samples for Poisson's ratio estimation were performed using Instron 5944 (Instron, Norwood, MA), a single-column table top mechanical testing system. Stress-relaxation measurements for the residual stress material (in the linear regime, at 2.5% strain), the creep compliance measurements for the rigid material (at 0.5 MPa stress), and the storage and loss modulus measurements (1 Hz cycling) for all of the materials were performed using DMA Q800 (TA Instruments, New Castle, DE). Differential scanning calorimetry measurements were performed using DSC Q100 (TA Instruments, New Castle, DE). Thickness measurements for the printed samples were performed using DektakXT stylus profilometer (Bruker Corp., Billerica, MA) and optical microscope SZ61 (Olympus Corp., Tokyo, Japan) fitted with SC30 3.3 MP microscope digital camera (Olympus Corp., Tokyo, Japan). The folding angles were measured using the Stream Start software (Olympus Corp., Tokyo, Japan) from the images taken using a Canon EOS 60D digital single-lens reflex (DSLR) camera and the SC30 microscope digital camera.

UV Intensity and Controlled Temperature Measurements. UV light intensities were measured using a Loctite UV A/B Radiometer Dosimeter (1390323; Loctite-Henkel, Düsseldorf, Germany). The broadband high-intensity UV source used was a F300 Heraeus system with the LC6B Benchtop conveyor (Fusion UV/Heraeus, Maryland). For the measurements of folding angles at controlled temperatures, a universal oven UF 30 (Memmert, Schwabach, Germany) is used to set up a controlled temperature atmosphere. To generate the hot air temperature variation for the samples with mechanical stops in Figure 5D, the hot air gun in X-tronic 5000 series rework station (Model #5040-XTS; X-tronic Int., Lincoln, NE) is used.

FTIR Measurements and Double-Bond Conversion. FTIR spectra were obtained using the Thermo Fischer FTIR 6700 Fourier transform infrared spectrometer setup in the attenuated total reflection (ATR) mode with a silicon crystal. The spectra were measured on three samples on the surface for each data point. The sample FTIR spectra are shown in Figure S2. The ratio between the absorbance of the vinyl group (809 cm^{-1}) with respect to the carbonyl group (1705 cm^{-1}) is used to measure the monomer conversion percentage similar to the technique used in a reference.[40] The reaction conversion is obtained by using the starting ink $(A_{vinyl}/A_{carbonyl})_{ink}$ as 0% conversion reference and the samples with four curing passes with the UV fusion $(A_{vinyl}/A_{carbonyl})_{UVfusion}$ as the fully cross-linked reference.

Self-Folding Electronic Composite Characterization and Video. The supply voltage for the electrochromic composite was provided using a Sourcemeter 2611B (Keithley Instruments, Cleveland, OH). Images and videos were recorded with Canon EOS 60D DSLR.

■ ASSOCIATED CONTENT

Ⓢ Supporting Information

The Supporting Information is available free of charge on the ACS Publications website at DOI: 10.1021/acsami.7b10443.

> Swelling of UV-cured polymer samples in different components (Figure S1); sample FTIR spectra (Figure S2); differential scanning calorimetry (DSC) and dynamic mechanical analysis (DMA) data (Figure S3); mechanical strain tests of the stress layer material (Figure S4); modeling the folding in the bilayer geometry (Figure S5); effect of heating and high UV dose on the folding behavior (Figure S6); design of the electronic composite (Figure S7); folding angle with stops (Figure S8); unfolding forces (Figure S9) (PDF)
> Video S1. Self-folded electrochromic device (MPG)
> Video S2. Unfolding experiments (MPG)

■ AUTHOR INFORMATION

Corresponding Author
*E-mail: subras@mit.edu.

ORCID Ⓓ
Subramanian Sundaram: 0000-0002-8456-916X
Ryan C. Hayward: 0000-0001-6483-2234

Author Contributions
S.S. conceived the project and was involved in all of the aspects of the work. S.S. and R.C.H. planned the experiments. D.S.K. helped with performing some characterization tests. S.S. wrote the manuscript with input from all of the authors. All of the authors discussed the results and read the manuscript.

Notes
The authors declare no competing financial interest.

■ ACKNOWLEDGMENTS

■ REFERENCES

(1) Whitesides, G. M.; Grzybowski, B. Self-Assembly at All Scales. *Science* **2002**, *295*, 2418−2421.

(2) Hawkes, E.; An, B.; Benbernou, N. M.; Tanaka, H.; Kim, S.; Demaine, E. D.; Rus, D.; Wood, R. J. Programmable Matter by Folding. *Proc. Natl. Acad. Sci. U.S.A.* **2010**, *107*, 12441−12445.

(3) Felton, S.; Tolley, M.; Demaine, E.; Rus, D.; Wood, R. A Method for Building Self-folding Machines. *Science* **2014**, *345*, 644−646.

(4) Guo, X.; Li, H.; Ahn, Y. B.; Duoss, E. B.; Hsia, K. J.; Lewis, J. A.; Nuzzo, R. G. Two- and Three-Dimensional Folding of Thin Film Single-Crystalline Silicon for Photovoltaic Power Applications. *Proc. Natl. Acad. Sci. U.S.A.* **2009**, *106*, 20149−20154.

(5) Hayes, G. J.; Liu, Y.; Genzer, J.; Lazzi, G.; Dickey, M. D. Self-Folding Origami Microstrip Antennas. *IEEE Trans. Antennas Propag.* **2014**, *62*, 5416−5419.

(6) Song, Y. M.; Xie, Y.; Malyarchuk, V.; Xiao, J.; Jung, I.; Choi, K.-J.; Liu, Z.; Park, H.; Lu, C.; Kim, R.-H.; Li, R.; Crozier, K. B.; Huang, Y.;

Rogers, J. A. Digital Cameras with Designs Inspired by the Arthropod Eye. *Nature* **2013**, *497*, 95−99.

(7) Zotov, S. A.; Rivers, M. C.; Trusov, A. A.; Shkel, A. M. Folded MEMS Pyramid Inertial Measurement Unit. *IEEE Sens. J.* **2011**, *11*, 2780−2789.

(8) Xu, S.; Yan, Z.; Jang, K.-I.; Huang, W.; Fu, H.; Kim, J.; Wei, Z.; Flavin, M.; McCracken, J.; Wang, R.; Badea, A.; Liu, Y.; Xiao, D.; Zhou, G.; Lee, J.; Chung, H. U.; Cheng, H.; Ren, W.; Banks, A.; Li, X.; Paik, U.; Nuzzo, R. G.; Huang, Y.; Zhang, Y.; Rogers, J. A. Assembly of Micro/Nanomaterials into Complex, Three-Dimensional Architectures by Compressive Buckling. *Science* **2015**, *347*, 154−159.

(9) Studart, A. R.; Erb, R. M. Bioinspired Materials that Self-Shape through Programmed Microstructures. *Soft Matter* **2014**, *10*, 1284−1294.

(10) Felton, S. M.; Tolley, M. T.; Shin, B.; Onal, C. D.; Demaine, E. D.; Rus, D.; Wood, R. J. Self-Folding with Shape Memory Composites. *Soft Matter* **2013**, *9*, 7688.

(11) Zhao, Q.; Zou, W.; Luo, Y.; Xie, T. Shape Memory Polymer Network with Thermally Distinct Elasticity and Plasticity. *Sci. Adv.* **2016**, *2*, No. e1501297.

(12) Overvelde, J. T. B.; de Jong, T. A.; Shevchenko, Y.; Becerra, S. A.; Whitesides, G. M.; Weaver, J. C.; Hoberman, C.; Bertoldi, K. A Three-Dimensional Actuated Origami-Inspired Transformable Metamaterial with Multiple Degrees of Freedom. *Nat. Commun.* **2016**, *7*, No. 10929.

(13) Na, J.-H.; Evans, A. A.; Bae, J.; Chiappelli, M. C.; Santangelo, C. D.; Lang, R. J.; Hull, T. C.; Hayward, R. J. Programming Reversibly Self-Folding Origami with Micropatterned Photo-Crosslinkable Polymer Trilayers. *Adv. Mater.* **2015**, *27*, 79−85.

(14) Mu, J.; Hou, C.; Wang, H.; Li, Y.; Zhang, Q.; Zhu, M. Origami-Inspired Active Graphene-based Paper for Programmable Instant Self-Folding Walking Devices. *Sci. Adv.* **2015**, *1*, No. e1500533.

(15) Blees, M. K.; Barnard, A. W.; Rose, P. A.; Roberts, S. P.; McGill, K. L.; Huang, P. Y.; Ruyack, A. R.; Kevek, J. W.; Kobrin, B.; Muller, D. A.; McEuen, P. L. Graphene Kirigami. *Nature* **2015**, *524*, 204−207.

(16) Scott, T. F.; Schneider, A. D.; Cook, W. D.; Bowman, C. N. Photoinduced Plasticity in Cross-Linked Polymers. *Science* **2005**, *308*, 1615−1617.

(17) Liu, Y.; Boyles, J. K.; Genzer, J.; Dickey, M. D. Self-Folding of Polymer Sheets using Local Light Absorption. *Soft Matter* **2012**, *8*, 1764−1769.

(18) Liu, Y.; Miskiewicz, M.; Escuti, M. J.; Genzer, J.; Dickey, M. D. Three-Dimensional Folding of Pre-Strained Polymer Sheets via Absorption of Laser Light. *J. Appl. Phys.* **2014**, *115*, No. 204911.

(19) Schmidt, O. G.; Eberl, K. Nanotechnology: Thin Solid Films Roll Up into Nanotubes. *Nature* **2001**, *410*, 168.

(20) Xu, B.; Hayward, R. C. Low-Voltage Switching of Crease Patterns on Hydrogel Surfaces. *Adv. Mater.* **2013**, *25*, 5555−5559.

(21) Ge, Q.; Qi, H.; Dunn, M. L. Active Materials by Four-Dimension Printing. *Appl. Phys. Lett.* **2013**, *103*, No. 131901.

(22) Raviv, D.; Zhao, W.; McKnelly, C.; Papadopoulou, A.; Kadambi, A.; Shi, B.; Hirsch, S.; Dikovsky, D.; Zyracki, M.; Olguin, C.; Raskar, R.; Tibbits, S. Active Printed Materials for Complex Self-Evolving Deformations. *Sci. Rep.* **2014**, *4*, No. 7422.

(23) Tibbits, S. 4D Printing: Multi-Material Shape Change. *Archit. Des.* **2014**, *84*, 116−121.

(24) Tumbleston, J. R.; Shirvanyants, D.; Ermoshkin, N.; Janusziewicz, R.; Johnson, A. R.; Kelly, D.; Chen, K.; Pinschmidt, R.; Rolland, J. P.; Ermoshkin, A.; Samulski, E. T.; DeSimone, J. M. Continuous Liquid Interface Production of 3D Objects. *Science* **2015**, *347*, 1349−1352.

(25) Ladd, C.; So, J.-H.; Muth, J.; Dickey, M. D. 3D Printing of Free Standing Liquid Metal Microstructures. *Adv. Mater.* **2013**, *25*, 5081−5085.

(26) Kolesky, D. B.; Truby, R. L.; Gladman, A.; Busbee, T. A.; Homan, K. A.; Lewis, J. A. 3D Bioprinting of Vascularized, Heterogeneous Cell-Laden Tissue Constructs. *Adv. Mater.* **2014**, *26*, 3124−3130.

(27) Eckel, Z. C.; Zhou, C.; Martin, J. H.; Jacobsen, A. J.; Carter, W. B.; Schaedler, T. A. Additive Manufacturing of Polymer-Derived Ceramics. *Science* **2016**, *351*, 58−62.

(28) Kokkinis, D.; Schaffner, M.; Studart, A. R. Multimaterial Magnetically Assisted 3D Printing of Composite Materials. *Nat. Commun.* **2015**, *6*, No. 8643.

(29) Mao, Y.; Yu, K.; Isakov, M. S.; Wu, J.; Dunn, M. L.; Qi, H. J. Sequential Self-Folding Structures by 3D Printed Digital Shape Memory Polymers. *Sci. Rep.* **2015**, *5*, No. 13616.

(30) Gladman, A. S.; Matsumoto, E. A.; Nuzzo, R. J.; Mahadevan, L.; Lewis, J. A. Biomimetic 4D Printing. *Nat. Mater.* **2016**, *15*, 413−418.

(31) Zhang, Q.; Zhang, K.; Hu, G. Smart Three-Dimensional Lightweight Structure Triggered From a Thin Composite Sheet via 3D Printing Technique. *Sci. Rep.* **2016**, *6*, No. 22431.

(32) Mao, Y.; Ding, Z.; Yuan, C.; Ai, S.; Isakov, M.; Wu, J.; Wang, T.; Dunn, M. L.; Qi, H. J. 3D Printed Reversible Shape Changing Components with Stimuli Responsive Materials. *Sci. Rep.* **2016**, *6*, No. 24761.

(33) Wu, J.; Yuan, C.; Ding, Z.; Isakov, M.; Mao, Y.; Wang, T.; Dunn, M. L.; Qi, H. J. Multi-Shape Active Composites by 3D Printing of Digital Shape Memory Polymers. *Sci. Rep.* **2016**, *6*, No. 24224.

(34) Ge, Q.; Sakhaei, A. H.; Lee, H.; Dunn, C. K.; Fang, N.; Dunn, M. L. Multimaterial 4D Printing with Tailorable Shape Memory Polymers. *Sci. Rep.* **2016**, *6*, No. 31110.

(35) Espalin, D.; Muse, D. W.; MacDonald, E.; Wicker, R. B. 3D Printing Multifunctionality: Structures with Electronics. *Int. J. Adv. Manuf. Technol.* **2014**, *72*, 963−978.

(36) Ota, H.; Emaminejad, S.; Gao, Y.; Zhao, A.; Wu, E.; Challa, S.; Chen, K.; Fahad, H. M.; Jha, A. K.; Kiriya, D.; Gao, W.; Shiraki, H.; Morioka, K.; Ferguson, A. R.; Healy, K. E.; Davis, R. W.; Javey, A. Application of 3D Printing for Smart Objects with Embedded Electronic Sensors and Systems. *Adv. Mater. Technol.* **2016**, *1*, No. 1600013.

(37) MacDonald, E.; Wicker, R. Multiprocess 3D Printing for Increasing Component Functionality. *Science* **2016**, *353*, No. aaf2093.

(38) Zarek, M.; Layani, M.; Cooperstein, I.; Sachyani, E.; Cohn, D.; Magdassi, S. 3D Printing of Shape Memory Polymers for Flexible Electronic Devices. *Adv. Mater.* **2016**, *28*, 4449−4454.

(39) Rodriguez, J. N.; Zhu, C.; Duoss, E. B.; Wilson, T. S.; Spadaccini, C. M.; Lewicki, J. P. Shape-Morphing Composites with Designed Micro-Architectures. *Sci. Rep.* **2016**, *6*, No. 27933.

(40) Huang, L.; Jiang, R.; Wu, J.; Song, J.; Bai, H.; Li, B.; Zhao, Q.; Xie, T. Ultrafast Digital Printing Toward 4D Shape Changing Materials. *Adv. Mater.* **2017**, *29*, No. 1605390.

(41) Ding, Z.; Yuan, C.; Peng, X.; Wang, T.; Qi, H. J.; Dunn, M. L. Direct 4D Printing via Active Composite Materials. *Sci. Adv.* **2017**, *3*, No. e1602890.

(42) Sundaram, S.; Jiang, Z.; Sitthi-Amorn, P.; Kim, D. S.; Baldo, M. A.; Matusik, W. 3D-Printed Autonomous Sensory Composites. *Adv. Mater. Technol.* **2017**, *2*, No. 1600257.

(43) Sitthi-Amorn, P.; Ramos, J. E.; Wangy, Y.; Kwan, J.; Lan, J.; Wang, W.; Matusik, W. MultiFab: A Machine Vision Assisted Platform for Multi-Material 3D Printing. *ACM Trans. Graphics* **2015**, *34*, 129:1−129:11.

(44) Glugla, D. J.; Alim, M. D.; Byars, K. D.; Nair, D. P.; Bowman, C. N.; Maute, K. K.; McLeod, R. R. Rigid Origami via Optical Programming and Deferred Self-Folding of a Two-Stage Photopolymer. *ACS Appl. Mater. Interfaces* **2016**, *8*, 29658−29667.

(45) Timoshenko, S. Analysis of Bi-Metal Thermostats. *J. Opt. Soc. Am.* **1925**, *11*, 233.

(46) Walker, S. B.; Lewis, J. A. Ink Composition for Making a Conductive Silver Structure. US 2015/0004325 A1, 2015.

(47) Andersson, P.; Nilsson, D.; Svensson, P.-O.; Chen, M.; Malmström, A.; Remonen, T.; Kugler, T.; Berggren, M. Active Matrix Displays Based on All-Organic Electrochemical Smart Pixels Printed on Paper. *Adv. Mater.* **2002**, *14*, 1460−1464.